EVLA Memo 207
Implementing Polarimetry with the JVLA's Low-Band Receivers

Rick Perley and Eric Greisen
National Radio Astronomy Observatory, Socorro, NM

April 11, 2019

Abstract

The JVLA's low-frequency receivers utilize linear polarization, and hence require different calibration and imaging procedures than those used with the circularly polarized receivers employed by the VLA at all other bands. This memo outlines the procedures needed for imaging and calibration using linearly-polarized systems at low frequencies. Observations of the moon demonstrate the correctness of these procedures.

1 Introduction and Motivation

The 'legacy' VLA employed circularly polarized receivers for all its observing bands, including 'P'-band (310 – 340 MHz). Although this system enabled polarimetry, there was little user interest in polarimetry at these frequencies, so that development of a calibration and imaging regimen was never seriously attempted.

The original VLA's P-band receivers proved to be incompatible with the JVLA's new electronics, so the decision was made to replace the old narrow-band receivers with wide-band amplifiers spanning 50 – 500 MHz. Due to the wide bandwidths, circular polarizers were not available, so these new low-frequency systems output linearly polarized signals – the only VLA receiver band to do so. Formation of the Stokes visibilities from a linearly polarized system is different than that from a circularly polarized one, so polarimetry with the VLA's P-band system requires some modification to the `AIPS` imaging software. In addition, enabling polarimetry at these low frequencies requires special calibration procedures, some distinctly different than those in use with circularly polarized systems.

Complicating the implementation of this new receiver system and the software is that polarimetric imaging at low frequencies is especially challenging. This is due to a combination of factors – a paucity of linearly polarized calibrators, a difficult RFI environment, relatively low sensitivity, and the strong Faraday rotation of the (weak) polarized signal at these frequencies, amongst others.

In this memo we describe the response of a linearly polarized system to polarized light, using a representative model of the antenna and electronics. The recovery of the Stokes' visibilities is described, and the calibration methodology outlined. Observations of unpolarized sources are used for basic gain calibration, observations of the polarized hotspots from the radio galaxies DA240 and 3C303 are used to determine the phase relation between parallel-hand signal chains, and observations of the Moon are used to confirm the various relationships and software.

2 Imaging Using Stokes Parameters

The Stokes parameters were defined by George Stokes in 1852 as a set of real values which describe the polarization state of electromagnetic radiation. Their use was extended to astronomy by Chandrasekhar. Here we define these parameters, and extend the definition to the complex visibilities needed in interferometric polarimetry.

2.1 Stokes Parameters

The response of any receiving system to partially polarized light can be analyzed in either a linear or circular basis. We choose to utilize the former, as the analysis is somewhat simpler since the feeds respond to the linear components of the electric field.

In the linear basis, we decompose the instantaneous electric field into its components in an orthogonal (x,y) frame. In accordance with IAU and IEEE conventions, the x-axis points to the NCP, and the y-axis points east. Utilizing

the quasi-monochromatic approximation (in which the bandwidths are finite and small compared to the average frequency – an approximation which is certainly well justified for our application), and expressing the components in terms of the complex 'analytic signals'[1] $\mathcal{E}_x$ and $\mathcal{E}_y$, the (real) Stokes parameters are defined by

$$\begin{aligned} I &= <\mathcal{E}_x\mathcal{E}_x^*> + <\mathcal{E}_y\mathcal{E}_y^*> & (1)\\ Q &= <\mathcal{E}_x\mathcal{E}_x^*> - <\mathcal{E}_y\mathcal{E}_y^*> & (2)\\ U &= <\mathcal{E}_x\mathcal{E}_y^*> + <\mathcal{E}_y\mathcal{E}_x^*> & (3)\\ iV &= <\mathcal{E}_x\mathcal{E}_y^*> - <\mathcal{E}_y\mathcal{E}_x^*> & (4) \end{aligned}$$

where the angle brackets imply averaging over a time long compared to the inverse bandwidth of the signal. Hence, I is the the sum of the powers in the two components, and Q the difference. U and iV are the sum and difference of cross-correlated signals.

These definitions apply to the field components at a single location, and it is easily shown that the relations given in equations 1 –4 result in real numbers for the Stokes parameters.

2.2 Stokes Visibilities

In interferometry, we exploit the Fourier transform relationship of the complex coherence of the electric fields in two different locations to the far-field brightness distribution which gives rise to these fields.

Denote the electric field's cartesian components at the two locations by $\mathcal{E}_{x1}$,$\mathcal{E}_{y1}$, and $\mathcal{E}_{x2}$, $\mathcal{E}_{y2}$. The four complex product combinations from these four signals are $<\mathcal{E}_{x1}\mathcal{E}_{x2}^*>$, $<\mathcal{E}_{x1}\mathcal{E}_{y2}^*>$, $<\mathcal{E}_{y1}\mathcal{E}_{x2}^*>$, and $<\mathcal{E}_{y1}\mathcal{E}_{y2}^*>$. By analogy with the definitions of the Stokes' parameters (equations 1 through 4), we define four complex Stokes visibilities $\mathcal{I}, \mathcal{Q}, \mathcal{U}, \mathcal{V}$ by:

$$\begin{aligned} \mathcal{I} &= <\mathcal{E}_{x1}\mathcal{E}_{x2}^*> + <\mathcal{E}_{y1}\mathcal{E}_{y2}^*> & (5)\\ \mathcal{Q} &= <\mathcal{E}_{x1}\mathcal{E}_{x2}^*> - <\mathcal{E}_{y1}\mathcal{E}_{y2}^*> & (6)\\ \mathcal{U} &= <\mathcal{E}_{x1}\mathcal{E}_{y2}^*> + <\mathcal{E}_{y1}\mathcal{E}_{x2}^*> & (7)\\ i\mathcal{V} &= <\mathcal{E}_{x1}\mathcal{E}_{y2}^*> - <\mathcal{E}_{y1}\mathcal{E}_{x2}^*> & (8) \end{aligned}$$

These Stokes visibilities are functions of the vector baseline between the two antennas, and are related to the four real brightness distributions I, Q, U, and V – functions of angle – , through Fourier transform:

$$\begin{aligned} I(l,m) &\iff \mathcal{I}(u,v) & (9)\\ Q(l,m) &\iff \mathcal{Q}(u,v) & (10)\\ U(l,m) &\iff \mathcal{U}(u,v) & (11)\\ V(l,m) &\iff \mathcal{V}(u,v) & (12) \end{aligned}$$

where (l,m) are the direction cosines defined w.r.t. the center of the region of interest (phase-tracking center), with l pointing north and m to the east, and (u,v) are the components of the baseline, measured in wavelengths, projected onto the plane perpendicular to the direction to the reference center[2]. In general, the Stokes visibilities are complex. Because the four Stokes brightnesses must be real, the corresponding visibilities are Hermitian. For a point source at the phase tracking center, the Stokes visibilites themselves are real.

If we could design a telescope whose output voltages are proportional to the linear components of the electric field, and orient it so that the feeds are correctly aligned on the sky, then the preceding equations would be all that are needed to recover the Stokes visibilities (with minor modifications to account for system gains). However, perfectly polarized systems are not possible in practice, and antennas and feeds are not normally aligned correctly, so we must develop a methodology for handling these more complex arrangements. The formalism to do so is developed in the next section.

[1]For a monochromatic sinusoidal signal $E_x = A_x\cos(\omega t)$, the analytic signal is defined as $\mathcal{E}_x = \sqrt{2}A_x e^{i\omega t}$. The amplitudes of the complex components are defined so as to allow interpretation of the products $<\mathcal{E}_x\mathcal{E}_x^*>$ and $<\mathcal{E}_y\mathcal{E}_y^*>$ to be the powers in the two orthogonal components.

[2]We ignore the complication that a baseline in general has a component perpendicular to this plane.

3 Imperfectly Polarized Antennas

Real systems comprise a series of components (antennas, amplifiers, downconverters, samplers, data transmission systems, etc.) each of which modifies the signal, and each of which imposes some imperfections onto the signals. To account for these effects, we employ the Jones' matrix formalism to relate the electric field components to the voltages presented to the correlator. Jones' matrix algebra is appropriate for a linear system of components, and should be an excellent approximation to reality for a well-designed radio telescope. The following description utilizes arbitrary polarization components, labelled p and q. In subsequent sections, the explicit relations for the linear basis will be given.

The relation between the input electric field components $\mathcal{E}_p$ and $\mathcal{E}_q$ and the two output voltages V_p and V_q from an arbitrarily polarized antenna[3] is written

$$\mathbf{V_{out}} = \mathbf{J}\mathcal{E}_{in} \tag{13}$$

where $\mathbf{V_{out}}$ and $\mathcal{E}_{in}$ are column vectors containing the two output voltages and the components of the input field, respectively. The Jones matrix $\mathbf{J}$ is a 2 x 2 matrix whose coefficients describe the amplitude and phase relations between the input electric fields and output voltages. All coefficients are considered complex.

$$\mathbf{J} = \begin{pmatrix} \alpha_{pp} & \alpha_{qp} \\ \alpha_{pq} & \alpha_{qq} \end{pmatrix} \tag{14}$$

The order of the subscripts is important – α_{pq} is the coupling coefficient from channel 'p' to channel 'q'.

The power in the Jones matrix formalism is that consecutive operations can be chained together, allowing easy analysis of complex systems. If the receiving system includes (say) pre-amplifiers, polarizers, and post-amplifiers, each described by its own Jones matrix, the entire system can then be characterized by a single Jones matrix, $\mathbf{J_c}$ which is the product of the component matrices:

$$\mathbf{J_c} = \mathbf{J_3}\mathbf{J_2}\mathbf{J_1} \tag{15}$$

The order of the matrix product is important – from right to left, following the propagation of the signal through the network.

Each antenna provides two voltage outputs, and the complex correlator produces all four products between the two antennas. The operation is described mathematically by (for one of the four combinations)

$$R_{p1p2} = < V_{p1} V_{p2}^* > . \tag{16}$$

Define the response vector $\mathbf{R}$ containing the four products

$$\mathbf{R} = \begin{pmatrix} R_{p1p2} \\ R_{p1q2} \\ R_{q1p2} \\ R_{q1q2} \end{pmatrix} \tag{17}$$

Similarly, define a 'Stokes Vector', containing the four possible correlations between the electric field's components:

$$\mathbf{S} = \begin{pmatrix} < \mathcal{E}_{p1} \mathcal{E}_{p2}^* > \\ < \mathcal{E}_{p1} \mathcal{E}_{q2}^* > \\ < \mathcal{E}_{q1} \mathcal{E}_{p2}^* > \\ < \mathcal{E}_{q1} \mathcal{E}_{q2}^* > \end{pmatrix} \tag{18}$$

The relation between the response vector $\mathbf{R}$ and the Stokes vector $\mathbf{S}$, is described by a 4 x 4 'polarization mixing matrix', often called the 'Mueller' matrix:

$$\mathbf{R} = \mathcal{M}\mathbf{S} \tag{19}$$

The sixteen terms in the matrix can be calculated through use of the 'outer product', or 'Kronecker product'. As described by Thompson, Moran, and Swenson, we have

$$\mathbf{R} = \mathbf{V_1} \otimes \mathbf{V_2^*} = \mathbf{J_1}\mathcal{E}_1 \otimes \mathbf{J_2^*}\mathcal{E}_2^* = (\mathbf{J_1} \otimes \mathbf{J_2^*})(\mathcal{E}_1 \otimes \mathcal{E}_2^*) = \mathcal{M}\mathbf{S}. \tag{20}$$

[3]It is to be understood that the p and q labels for the electric field denote the field components in the chosen basis. For the output voltages, these labels are nominal only, as these voltages comprise contributions from both polarizations.

where I have used the useful property of the outer product: $\mathbf{A_1 B_1} \otimes \mathbf{A_2^* B_2^*} = (\mathbf{A_1} \otimes \mathbf{A_2^*})(\mathbf{B_1} \otimes \mathbf{B_2^*})$.

The 4 x 4 matrix $\mathcal{M} = \mathbf{J_1} \otimes \mathbf{J_2^*}$ is

$$\mathcal{M} = \begin{pmatrix} \alpha_{pp1}\alpha^*_{pp2} & \alpha_{pp1}\alpha^*_{qp2} & \alpha_{qp1}\alpha^*_{pp2} & \alpha_{qp1}\alpha^*_{qp2} \\ \alpha_{pp1}\alpha^*_{pq2} & \alpha_{pp1}\alpha^*_{qq2} & \alpha_{qp1}\alpha^*_{pq2} & \alpha_{qp1}\alpha^*_{qq2} \\ \alpha_{pq1}\alpha^*_{pp2} & \alpha_{pq1}\alpha^*_{qp2} & \alpha_{qq1}\alpha^*_{pp2} & \alpha_{qq1}\alpha^*_{qp2} \\ \alpha_{pq1}\alpha^*_{pq2} & \alpha_{pq1}\alpha^*_{qq2} & \alpha_{qq1}\alpha^*_{pq2} & \alpha_{qq1}\alpha^*_{qq2} \end{pmatrix} \tag{21}$$

The complex coefficients α are the Jones' matrix elements defined in equation 14. Note that if the antenna Jones matrix is the product of individual component matrices, the resulting polarization mixing matrix is also the product of the individual polarization mixing matrices, taken in the same order:

$$\mathcal{M} = \mathcal{M}_3 \mathcal{M}_2 \mathcal{M}_1 \tag{22}$$

3.1 Solving for the Stokes' Vector

We have (equation 19) for the 'Measurement Equation':

$$\mathbf{R} = \mathcal{M}\mathbf{S} \tag{23}$$

The formal solution for $\mathbf{S}$ is given by

$$\mathbf{S} = \mathcal{M}^{-1}\mathbf{R} \tag{24}$$

The problem is then to invert the matrices. For diagonal matrices, the process is elementary: the four elements are replaced by their inverses. Thus, the inverse of the diagonal gain matrix

$$\mathbf{G} = \begin{pmatrix} G_{p1}G^*_{p2} & 0 & 0 & 0 \\ 0 & G_{p1}G^*_{q2} & 0 & 0 \\ 0 & 0 & G_{q1}G^*_{p2} & 0 \\ 0 & 0 & 0 & G_{q1}G^*_{q2} \end{pmatrix} \tag{25}$$

is

$$\mathbf{G}^{-1} = \begin{pmatrix} \frac{1}{G_{p1}G^*_{p2}} & 0 & 0 & 0 \\ 0 & \frac{1}{G_{p1}G^*_{q2}} & 0 & 0 \\ 0 & 0 & \frac{1}{G_{q1}G^*_{p2}} & 0 \\ 0 & 0 & 0 & \frac{1}{G_{q1}G^*_{q2}} \end{pmatrix} \tag{26}$$

For non-diagonal matrices, the inversion is most easily done by using another property of the outer product, that if

$$\mathbf{M} = \mathbf{A} \otimes \mathbf{B} \tag{27}$$

then

$$\mathbf{M}^{-1} = \mathbf{A}^{-1} \otimes \mathbf{B}^{-1} \tag{28}$$

Thus, for a general 2 x 2 complex matrix

$$\mathbf{J} = \begin{pmatrix} \alpha_{pp} & \alpha_{qp} \\ \alpha_{pq} & \alpha_{qq} \end{pmatrix} \tag{29}$$

whose inversion is

$$\mathbf{J}^{-1} = \frac{1}{\alpha_{pp}\alpha_{qq} - \alpha_{qp}\alpha_{pq}} \begin{pmatrix} \alpha_{qq} & -\alpha_{qp} \\ -\alpha_{pq} & \alpha_{pp} \end{pmatrix} \tag{30}$$

the 4 x 4 outer product

$$\mathcal{M} = \mathbf{J}_1 \otimes \mathbf{J}_2^* = \begin{pmatrix} \alpha_{pp1}\alpha^*_{pp2} & \alpha_{pp1}\alpha^*_{qp2} & \alpha_{qp1}\alpha^*_{pp2} & \alpha_{qp1}\alpha^*_{qp2} \\ \alpha_{pp1}\alpha^*_{pq2} & \alpha_{pp1}\alpha^*_{qq2} & \alpha_{qp1}\alpha^*_{pq2} & \alpha_{qp1}\alpha^*_{qq2} \\ \alpha_{pq1}\alpha^*_{pp2} & \alpha_{pq1}\alpha^*_{qp2} & \alpha_{qq1}\alpha^*_{pp2} & \alpha_{qq1}\alpha^*_{qp2} \\ \alpha_{pq1}\alpha^*_{pq2} & \alpha_{pq1}\alpha^*_{qq2} & \alpha_{qq1}\alpha^*_{pq2} & \alpha_{qq1}\alpha^*_{qq2} \end{pmatrix} \tag{31}$$

has an inverse given by

$$\mathcal{M}^{-1} = \mathbf{J}_1^{-1} \otimes \mathbf{J}_2^{*-1} = N \begin{pmatrix} \alpha_{qq1}\alpha^*_{qq2} & -\alpha_{qq1}\alpha^*_{qp2} & -\alpha_{qp1}\alpha^*_{qq2} & \alpha_{qp1}\alpha^*_{qp2} \\ -\alpha_{qq1}\alpha^*_{pq2} & \alpha_{qq1}\alpha^*_{pp2} & \alpha_{qp1}\alpha^*_{pq2} & -\alpha_{qp1}\alpha^*_{pp2} \\ -\alpha_{pq1}\alpha^*_{qq2} & \alpha_{pq1}\alpha^*_{qp2} & \alpha_{pp1}\alpha^*_{qq2} & -\alpha_{pp1}\alpha^*_{qp2} \\ \alpha_{pq1}\alpha^*_{pq2} & -\alpha_{pq1}\alpha^*_{pp2} & -\alpha_{pp1}\alpha^*_{pq2} & \alpha_{pp1}\alpha^*_{pp2} \end{pmatrix} \tag{32}$$

where N is a normalizing factor:

$$N = \frac{1}{(\alpha_{pp1}\alpha_{qq1} - \alpha_{qp1}\alpha_{pq1})(\alpha^*_{pp2}\alpha^*_{qq2} - \alpha^*_{qp2}\alpha^*_{pq2})} \tag{33}$$

4 Application – The VLA's LowBand System

Application of the concepts presented in Section 3 to the VLA's low-frequency receiving system is straightforward. Each stage of the receiving system is modelled with a Jones matrix, from which the relationships between the correlator output and Stokes' visibilities can be determined.

4.1 The Model for the VLA's Low-band System

It is assumed that each dipole responds primarily to the electric field component parallel to the position angle of that dipole, and provides a voltage which is subsequently amplified by a series of amplifiers and transported to the correlator. We also assume that the two dipoles are orthogonal, and are rotated by angle θ with respect to the antenna frame. This mis-orientation can be different for each antenna. It is also assumed that all antennas are identically oriented on the sky, so that a single parallactic angle[4] Ψ_p describes the antenna orientation with respect to the sky frame.[5] Thus, the orientation of the vertical dipole w.r.t. the astronomical frame is given by $\Psi = \Psi_p + \theta$. The relationships of these angles to the two frames are shown in Figure 1.

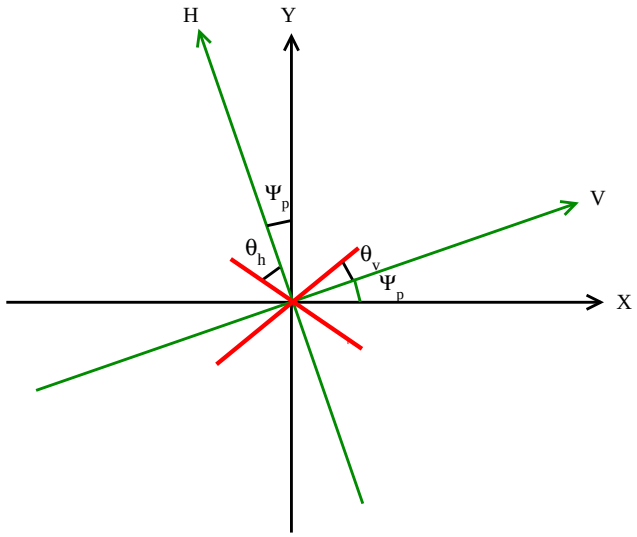

Figure 1: Showing the dipole orientation angles. The antenna dipoles are shown by the short red lines. The antenna coordinate frame (v,h) (green) is rotated by the parallactic angle Ψ_p with respect to the sky (x,y) frame. Angles θ_v and θ_h are the misalignments of the vertical and horizontal dipoles w.r.t. the antenna frame. In this treatment, we assume the misorientations are equal, so that $\theta_v = \theta_h = \theta$

Designate by $\mathcal{E}_x$ and $\mathcal{E}_y$ the analytic signals describing the (x,y) components of the (real) electric fields at the antenna. Thus, $\mathcal{E}_x$ is the electric field component aligned with the direction to the NCP, while $\mathcal{E}_y$ is that component aligned with the E-W direction.

[4] $\sin\Psi_p = \sin A \cos l / \cos\delta$, where l is the latitude, A is the source azimuth, and δ is the source declination. Note that the source azimuth A is defined CCW w.r.t. north, so that Ψ_p is positive for positive hour angles.

[5] This is a sufficient approximation for the VLA, as all antenna pads are oriented (more or less) so that the antennas' azimuth axes are parallel.

The voltages induced by these fields at the output of the dipoles are then

$$V_v = G_v[\mathcal{E}_x \cos\Psi + \mathcal{E}_y \sin\Psi] \quad (34)$$

$$V_h = G_h[-\mathcal{E}_x \sin\Psi + \mathcal{E}_y \cos\Psi] \quad (35)$$

where G_h and G_v are gains due to the dipole, cables, and amplifiers, plus any effects from the collecting area of the antenna reflector, and $\Psi = \Psi_p + \theta$ is the orientation of the vertical dipole w.r.t. the sky frame.

In terms of Jones matrices, we write

$$\mathbf{V} = \mathbf{G}\mathbf{J_{ori}}\mathcal{E} \quad (36)$$

where the orientation matrix $\mathbf{J_{ori}}$ is defined by

$$\mathbf{J_{ori}} = \begin{pmatrix} \cos\Psi & \sin\Psi \\ -\sin\Psi & \cos\Psi \end{pmatrix} \quad (37)$$

the electronic gains matrix $\mathbf{G}$ is

$$\mathbf{G} = \begin{pmatrix} G_v & 0 \\ 0 & G_h \end{pmatrix} \quad (38)$$

and $\mathbf{V}$ and $\mathcal{E}$ are 1 x 2 column vectors describing the voltages and analytic fields for the two components.

It will be useful to distinguish between the orientations due to parallactic angle and misalignment angles:

$$\mathbf{J_{ori}} = \mathbf{J_{mis}}\mathbf{J_{par}} \quad (39)$$

where the dipole misorientation is described by

$$\mathbf{J_{mis}} = \begin{pmatrix} \cos\theta & \sin\theta \\ -\sin\theta & \cos\theta \end{pmatrix} \quad (40)$$

and the parallactic angle rotation by

$$\mathbf{J_{par}} = \begin{pmatrix} \cos\Psi_p & \sin\Psi_p \\ -\sin\Psi_p & \cos\Psi_p \end{pmatrix} \quad (41)$$

It is easily shown that these operations commute: $\mathbf{J_{mis}}\mathbf{J_{par}} = \mathbf{J_{par}}\mathbf{J_{mis}}$. [6] It is physically reasonable to make this separation, as the parallactic angle is a known variable, whose effects can be accounted for when forming the visibilities, while the dipole misorientation is in general unknown, and has been shown to vary over timescales of days. Hence, its value must be found as part of calibration.

However, our model is not yet sufficient, as the two orthogonal dipoles are not completely electrically isolated. For various reasons, a single input linearly polarized electric field oriented with one dipole will weakly couple with the orthogonal dipole. We describe this phenomenon with a cross-polarization, or 'D-term' matrix:

$$\mathbf{J_D} = \begin{pmatrix} 1 & D_{hv} \\ D_{vh} & 1 \end{pmatrix} \quad (42)$$

In general, the diagonal terms should not be unity, as the coupling of a signal from, say the 'V' channel into the 'H' channel must be accompanying by a loss of amplitude in the 'V' channel – i.e., the diagonal elements should be listed as D_{vv} and D_{hh}. However, as these can be considered parallel-hand gain terms, we choose to use this normalized form for simplicity.

Both the misalignment and 'D-term' factors describe leakages of signals from one polarization channel to another. Since in our model these two effects are consecutive, they are most conveniently considered together. With the presumption that the coupling follows the misalignment, we can combine the two to form a single cross-polarization Jones matrix: $\mathbf{J_X} = \mathbf{J_D}\mathbf{J_{mis}}$. We have:

$$\mathbf{J_X} = \begin{pmatrix} \cos\theta - D_{hv}\sin\theta & \sin\theta + D_{hv}\cos\theta \\ D_{vh}\cos\theta - \sin\theta & D_{vh}\sin\theta + \cos\theta \end{pmatrix} \quad (43)$$

[6] Note that is is true only if the dipoles are orthogonal.

We now assume the dipoles are close to proper alignment, so that $\sin\theta \ll 1$. Since the 'D' terms are also very small, we can ignore second order products, and factor out the constant $\cos\theta$ term to obtain:

$$\mathbf{J_X} = \cos\theta \begin{pmatrix} 1 & T_{hv} \\ T_{vh} & 1 \end{pmatrix} \tag{44}$$

where for notational simplicity, we have substituted $T_{hv} = D_{hv} + \tan\theta$, and $T_{vh} = D_{vh} - \tan\theta$. The $\cos\theta$ term will be absorbed into the parallel-hand gains, and we ignore it from here on.

The last stage in our model is the parallel hand gain, represented by complex gain factors:

$$\mathbf{J_G} = \begin{pmatrix} G_v & 0 \\ 0 & G_h \end{pmatrix} \tag{45}$$

Thus, our complete model, sufficient for the purpose intended, is given by:

$$\mathbf{R} = \mathcal{M}\mathbf{S} = \mathbf{J_G J_X J_{par} S} \tag{46}$$

4.2 Cross-Correlations – The Mueller Matrices

The preceding development is applicable to a single antenna. When considering the response of the interferometer to polarized radiation, we must deal with the 4 x 4 Mueller matrix generated by the outer product between the two corresponding Jones' matrices, as described in Section 3. Each Jones' matrix pair (one for each antenna) generates a corresponding Mueller matrix. For the Jones' gain matrices $\mathbf{J_{G1}}$ and $\mathbf{J_{G2}}$ – where the numerical indices refer to the two antennas – we have for its Mueller matrix $\mathcal{M}_G$

$$\mathcal{M}_G = \begin{pmatrix} G_{v1}G^*_{v2} & 0 & 0 & 0 \\ 0 & G_{v1}G^*_{h2} & 0 & 0 \\ 0 & 0 & G_{h1}G^*_{v2} & 0 \\ 0 & 0 & 0 & G_{h1}G^*_{h2} \end{pmatrix} \tag{47}$$

The misalignment/leakage Mueller matrix is the outer product of the Jones matrices given in equation 44:

$$\mathcal{M}_{mis} = \begin{pmatrix} 1 & T^*_{hv2} & T_{hv1} & T_{hv1}T^*_{hv2} \\ T^*_{vh2} & 1 & T_{hv1}T^*_{vh2} & T_{hv1} \\ T_{vh1} & T_{vh1}T^*_{hv2} & 1 & T^*_{hv2} \\ T_{vh1}T^*_{vh2} & T_{vh1} & T^*_{vh2} & 1 \end{pmatrix} \tag{48}$$

For the parallactic Mueller matrix, we have (from eqn 41):

$$\mathcal{M}_{par} = \begin{pmatrix} \cos^2\Psi_p & \cos\Psi_p\sin\Psi_p & \sin\Psi_p\cos\Psi_p & \sin^2\Psi_p \\ -\cos\Psi_p\sin\Psi_p & \cos^2\Psi_p & -\sin^2\Psi_p & \sin\Psi_p\cos\Psi_p \\ -\sin\Psi_p\cos\Psi_p & -\sin^2\Psi_p & \cos^2\Psi_P & \cos\Psi_p\sin\Psi_p \\ \sin^2\Psi_p & -\sin\Psi_p\cos\Psi_p & -\cos\Psi_p\sin\Psi_p & \cos^2\Psi_p \end{pmatrix} \tag{49}$$

where for notational simplicity, we assume the two antennas have the same parallactic angle.

4.3 The Inversions – Solving for the Stokes Vector

The measurement equation is (eqn 46)

$$\mathbf{R} = \mathcal{M}_G\mathcal{M}_X\mathcal{M}_{par}\mathbf{S} \tag{50}$$

The solution is

$$\mathbf{S} = \mathcal{M}^{-1}_{par}\mathcal{M}^{-1}_X\mathcal{M}^{-1}_G\mathbf{R} \tag{51}$$

where the response vector $\mathbf{R}$ is

$$\mathbf{R} = \begin{pmatrix} R_{v1v2} \\ R_{v1h2} \\ R_{h1v2} \\ R_{h1h2} \end{pmatrix} \tag{52}$$

and **S** is the Stokes vector for a linear basis (from eqn 5 – 8 and eqn 18):

$$\mathbf{S_L} = \begin{pmatrix} (\mathcal{I}+\mathcal{Q})/2 \\ (\mathcal{U}+i\mathcal{V})/2 \\ (\mathcal{U}-i\mathcal{V})/2 \\ (\mathcal{I}-\mathcal{Q})/2 \end{pmatrix} \tag{53}$$

The inverse of the gain matrix, (eqn 47) is, using eqn 26:

$$\mathcal{M}_G^{-1} = \begin{pmatrix} \frac{1}{G_{v1}G_{v2}^*} & 0 & 0 & 0 \\ 0 & \frac{1}{G_{v1}G_{h2}^*} & 0 & 0 \\ 0 & 0 & \frac{1}{G_{h1}G_{v2}^*} & 0 \\ 0 & 0 & 0 & \frac{1}{G_{h1}G_{h2}^*} \end{pmatrix} \tag{54}$$

The inverse of the cross-polarization matrix (equation 48) is, using eqn 32

$$\mathcal{M}_X^{-1} = \frac{1}{N}\begin{pmatrix} 1 & -T_{hv2}^* & -T_{hv1} & T_{hv1}T_{hv2}^* \\ -T_{vh2}^* & 1 & T_{hv1}T_{vh2}^* & -T_{hv1} \\ -T_{vh1} & T_{vh1}T_{hv2}^* & 1 & -T_{hv2}^* \\ T_{vh1}T_{vh2}^* & -T_{vh1} & -T_{vh2}^* & 1 \end{pmatrix} \tag{55}$$

where the normalizing factor is $N = (1 - T_{hv1}T_{vh1})(1 - T_{hv2}^*T_{vh2}^*)$. The inversion of the parallactic angle matrix is

$$\mathcal{M}_{par}^{-1} = \begin{pmatrix} \cos^2\Psi_p & -\cos\Psi_p\sin\Psi_p & -\sin\Psi_p\cos\Psi_p & \sin^2\Psi_p \\ \cos\Psi_p\sin\Psi_p & \cos^2\Psi_p & -\sin^2\Psi_p & -\sin\Psi_p\cos\Psi_p \\ \sin\Psi_p\cos\Psi_p & -\sin^2\Psi_p & \cos^2\Psi_P & -\cos\Psi_p\sin\Psi_p \\ \sin^2\Psi_p & \sin\Psi_p\cos\Psi_p & \cos\Psi_p\sin\Psi_p & \cos^2\Psi_p \end{pmatrix} \tag{56}$$

All that is needed is to determine the values of the gains and leakage factors. There are eight complex factors (four gains and four leakages), plus one real number – the misalignment angle, for each antenna.

5 Calibration

Equation 51 gives the prescription for generating the desired Stokes visibilities from the observed correlations. Doing so requires determination of the calibration quantities, for which we utilize equation 50 for sources whose Stokes visibilities are known.

To illustrate the complexity of this, we first expand equation 50 (the 'measurement equation') for general radiation from an arbitrary source for our simple model:

$$\begin{aligned}
R_{v_1v_2} &= G_{v1}G_{v2}^*\{\mathcal{I}[1+T_{hv1}T_{hv2}^*] + \mathcal{Q}[\cos 2\Psi_p(1-T_{hv1}T_{hv2}^*) - \sin 2\Psi_p(T_{hv2}^*+T_{hv1})] + \\
&\quad \mathcal{U}[\sin 2\Psi_p(1-T_{hv1}T_{hv2}^*) + \cos 2\Psi_p(T_{hv2}^*+T_{hv1})] + i\mathcal{V}[T_{hv2}^*-T_{hv1}]\}/2 \qquad (57)\\
R_{v_1h_2} &= G_{v1}G_{h2}^*\{\mathcal{I}[T_{hv1}+T_{vh2}^*)] + \mathcal{Q}[\cos 2\Psi_p(T_{hv2}^*-t_{hv1}) - \sin 2\Psi_p(1+T_{hv1}^*+T_{vh2}^*)] + \\
&\quad \mathcal{U}[\sin 2\Psi_p(T_{vh2}^*-T_{hv1}) + \cos 2\Psi_p(1+T_{hv1}T_{hv2}^*)] + i\mathcal{V}[1-T_{hv1}T_{vh2}^*]\}/2 \qquad (58)\\
R_{h_1v_2} &= G_{h1}G_{v2}^*\{\mathcal{I}[T_{vh1}+T_{hv2}^*)] + \mathcal{Q}[\cos 2\Psi_p(T_{vh1}-T_{hv2}^*) - \sin 2\Psi_p(1+T_{vh1}+T_{hv2}^*)] + \\
&\quad \mathcal{U}[\sin 2\Psi_p(T_{vh1}-T_{hv2}^*) + \cos 2\Psi_p(1+T_{vh1}T_{hv2}^*)] - i\mathcal{V}[1-T_{vh1}T_{hv2}^*]\}/2 \qquad (59)\\
R_{h_1h_2} &= G_{h1}G_{h2}^*\{\mathcal{I}[1+T_{vh1}T_{vh2}^*)] - \mathcal{Q}[\cos 2\Psi_p(1-T_{vh1}T_{vh2}^*) + \sin 2\Psi_p(T_{vh1}+T_{vh2}^*)] - \\
&\quad \mathcal{U}[\sin 2\Psi_p(1-T_{vh1}T_{vh2}^*) - \cos 2\Psi_p(T_{vh1}+T_{vh2}^*)] + i\mathcal{V}[T_{vh1}-T_{vh2}^*]\}/2 \qquad (60)
\end{aligned}$$

Note that, for an unresolved calibrator at the phase center, the complex visibilities $\mathcal{I}, \mathcal{Q}, \mathcal{U}$, and $\mathcal{V}$ become the scalars I, Q, U, and V.

5.1 Parallel-Hand Gains

This is a rather fearsome set of equations from which to determine the calibration constants. But there is no need to utilize this set – calibration can never be precise for a number of reasons, and what is important is to identify the major factors which are needed to give sufficiently accurate calibration for the science.

The first level of simplication comes from noting that the 'T' terms and the normalized polarized Stokes values (Q/I, U/I, V/I) for the calibrator sources are all much smaller than unity. Ignoring all second order products (T with T, and T with Q/I, U/I, and V/I) gives us a considerably simpler set:

$$\begin{aligned}
R_{v_1 dv_2} &= G_{v1}G^*_{v2}[\mathcal{I} + \mathcal{Q}\cos 2\Psi_p + \mathcal{U}\sin 2\Psi_P]/2 &(61)\\
R_{v_2 h_2} &= G_{v1}G^*_{h2}[\mathcal{I}(T_{hv1} + T^*_{vh2}) - \mathcal{Q}\sin 2\Psi_p + \mathcal{U}\cos 2\Psi_p + i\mathcal{V}]/2 &(62)\\
R_{h_1 v_2} &= G_{h1}G^*_{v2}[\mathcal{I}(T_{vh1} + T^*_{hv2}) - \mathcal{Q}\sin 2\Psi_p + \mathcal{U}\cos 2\Psi_p - i\mathcal{V}]/2 &(63)\\
R_{h_1 h_2} &= G_{h1}G^*_{h2}[\mathcal{I} - \mathcal{Q}\cos 2\Psi_p - \mathcal{U}\sin 2\Psi_p]/2 &(64)
\end{aligned}$$

which is the set normally employed for calibration purposes. Clearly, it is the parallel-hand correlations that are to be used in determing the parallel-hand gains. For these, including the misalignment angles gives us a only slightly more complicated set:

$$\begin{aligned}
R_{v1v2} &= G_{v1}G^*_{v2}[\mathcal{I}\cos(\Delta\theta) + \mathcal{Q}\cos(2\Psi_p + \Sigma\theta) + \mathcal{U}\sin(2\Psi_p + \Sigma\theta) - i\mathcal{V}\sin(\Delta\theta)]/2 &(65)\\
R_{h1h2} &= G_{h1}G^*_{h2}[\mathcal{I}\cos(\Delta\theta) - \mathcal{Q}\cos(2\Psi_p + \Sigma\theta) - \mathcal{U}\sin(2\Psi_p + \Sigma\theta) - i\mathcal{V}\sin(\Delta\theta)]/2 &(66)
\end{aligned}$$

The parallel hand responses have amplitudes which vary sinusoidally with parallactic angle about a mean value proportional to $\mathcal{I}\cos(\Delta\theta)/2$. Ignoring the Stokes V contribution (generally an excellent approximation) the amplitude of the sinusoidal variation is proportional to $P = \sqrt{Q^2 + U^2}$, the total linearly polarized flux. In general, if the values of Q and U are not known in advance (nearly always the case), they must be derived from the data by fitting for P and phase angle $\beta = \arctan(U/Q)$. This requires an observation long enough to provide a sufficient change in parallactic angle to allow separation of the linearly polarized flux contribution from the total intensity. However, at low frequencies, this might not be sufficient for a clean determination of the calibrator polarization, as the ionosphere rotates the plane of polarization over time. The typical ionospheric RM (rotation measure) is about 1 radian/m^2, so the plane of polarized emission will typically be rotated at 327 MHz by about 50 degrees, and is likely to vary by tens of degrees over the course of the day. This effect makes gain calibration with polarized sources very uncertain.

Calibration is very much simplified if the sources employed are unpolarized. This is an emanently practical approximation, as it appears that nearly all the standard calibrators are indeed unpolarized at meter wavelengths. With this approximation, we write down the general relations for this case:

$$\begin{aligned}
R_{v_1 v_2} &= G_{v1}G^*_{v2}\mathcal{I}(1 + T_{hv1}T^*_{hv2})/2 &(67)\\
R_{v_1 h_2} &= G_{v1}G^*_{h2}\mathcal{I}(T_{hv1} + T^*_{vh2})/2 &(68)\\
R_{h_1 v_2} &= G_{h1}G^*_{v2}\mathcal{I}(T_{vh1} + T^*_{hv2})/2 &(69)\\
R_{h_1 h_2} &= G_{h1}G^*_{h2}\mathcal{I}(1 + T_{vh1}T^*_{vh2})/2 &(70)
\end{aligned}$$

Including the misalignments, we have (for the parallel-hands):

$$\begin{aligned}
R_{v1v2} &= \frac{G_{v1}G^*_{v2}}{2}\mathcal{I}\cos(\Delta\theta) &(71)\\
R_{h1h2} &= \frac{G_{h1}G^*_{h2}}{2}\mathcal{I}\cos(\Delta\theta) &(72)
\end{aligned}$$

The process of parallel hand gain solution is generally through a least-squares solution for the voltage amplitude gains, and the phase differences w.r.t. the reference antenna. Application of these gains separately calibrates the 'V' and 'H' signal channels, but there will in general remain a phase offset *between* these two signal chains.

The frequency dependence of the parallel-hand gains is not explictly addressed in the treatment above. In practice, frequency variations in the gains (including both amplitude and phase) are solved for each frequency channel as part of the bandpass calibration. This includes the delay solution – which shows up as a linear slope in the phase w.r.t. frequency.

5.2 Cross-Hand Delay

Parallel-hand (regular) calibration will correctly adjust the data for all factors (amplitude, phase, delay) affecting the parallel hand (HH and VV) signal chains. If the goal of the observations only requires the Stokes 'I' image, this is all the calibration that is required. However if the science goals require measurement of the polarization (Stokes Q, U, and V), further calibration is needed, as these require use of the cross-hand ('VH' and 'HV') correlations.

In this case, the remaining factors needing calibration involve the cross-correlations between these signal chains – cross-hand phase, cross-hand delay, dipole mis-orientation, and the 'leakage' terms. We discuss the cross-hand delay first.

The parallel-hand calibration process will remove any differences in propagation delay beween the antennas in the two parallel-hand signal chains, but is insensitive to the signal propagation delay difference *between* the two signal chains. After application of the parallel-hand gains, this cross-hand delay is that of the reference antenna. Removing it requires use of the cross-hand response. Presuming the parallel-hand gains have been applied, we have, for the cross-hand responses (where we have ignored the 'D' leakage terms):

$$R_{v1h2} = [\mathcal{I}\sin(\Delta\theta) - \mathcal{Q}\sin(2\Psi_p + \Sigma\theta) + \mathcal{U}\cos(2\Psi_p + \Sigma\theta) + i\mathcal{V}\cos(\Delta\theta)]/2 \quad (73)$$

$$R_{h1v2} = [-\mathcal{I}\sin(\Delta\theta) - \mathcal{Q}\sin(2\Psi_p + \Sigma\theta) + \mathcal{U}\cos(2\Psi_p + \Sigma\theta) - i\mathcal{V}\cos(\Delta\theta)]/2 \quad (74)$$

It is evident that in order to calibrate the cross-hand correlations, we need to have a strongly polarized source (non-zero Q, U, or V), or, misaligned dipoles ($\Delta\theta \neq 0$). At meter-wavelengths, nearly all calibrator sources are negligibly polarized, so we restrict our attention to the latter case.

For a non-polarized source, there is no signal with which to calibrate and remove the cross-hand phases, unless one or more dipoles are misoriented. In this case, we have (presuming the parallel-hand gains have been applied)

$$R_{v1h2} = [\mathcal{I}\sin(\Delta\theta)]/2 \quad (75)$$

$$R_{h1v2} = [-\mathcal{I}\sin(\Delta\theta)]/2 \quad (76)$$

(Note that the negative sign in equation 76 merely means the phases are offset by π radians.)

The delay shows up as a phase slope in the cross-hand responses, (the phase slope in the 'HV' channel has the opposite sign to that in the 'VH' channel), and can be easily measured in the same manner as that done for the parallel-hand delays. Although it may seem desirable to pick an antenna known to be misaliged as the reference, in fact this is not advisable for reasons noted later. It appears that in practice, it suffices that one or two non-reference antennas be misaligned by small amounts to provide sufficient signal to measure the cross-hand delay.

5.3 Cross-Hand Phase Calibration

But we are not quite done. The regimen noted above will correctly remove all the effects of cross-hand delay, but leaves one parameter undetermined – that of the cross-hand phase. This is not removed by the cross-hand delay calibration, as the phase paths through electronic signal chains in the two parallel hand channels are not necessarily identical – even though their delays may be. In the absence of a specially designed cross-hand calibration system, removal of this residual phase *requires* a polarized calibrator.

It is useful to calculate the observational effect of the phase offset between the parallel-hand channels. Let us assume that the misorientation of the dipoles and the cross-polarization ('D'-terms) are negligible, and that the parallel hand calibration and cross-hand delays have been determined and applied. Then, the only remaining term is a cross hand phase, denoted ϕ, corresponding to the phase offset of the 'H' channel with respect to the 'V' channel. The responses for the cross-hand correlations can then be written (from eqn 62 and 63):

$$2R'_{v1h2} = e^{-i\phi}[-\mathcal{Q}\sin(2\Psi_p) + \mathcal{U}\cos(2\Psi_p) + i\mathcal{V}] \quad (77)$$

$$2R'_{h1v2} = e^{i\phi}[-\mathcal{Q}\sin(2\Psi_p) + \mathcal{U}\cos(2\Psi_p) - i\mathcal{V}] \quad (78)$$

where the 'prime' denotes the calibrated visibilities, absent the cross-hand phase. Note that these equations retain the form appropriate for the antenna frame – *i.e.* they have not been corrected for the effect of parallactic angle. The parallel-hand responses are unaffected by the phase offset, so retain the form given in equations 61 and 64.

If the Stokes visibilities are then generated without applying a counter-rotation to offset the known parallactic angle, the following relations are found beween the true Stokes visibilities and the derived (denoted by primes) ones ($\mathcal{I}$', $\mathcal{Q}$', $\mathcal{U}$', $\mathcal{V}$')

$$\mathcal{I}' = \mathcal{I} \quad (79)$$

$$\mathcal{Q}' = \mathcal{Q}\cos 2\Psi_p + \mathcal{U}\sin 2\Psi_p \quad (80)$$

$$\mathcal{U}' = (-\mathcal{Q}\sin 2\Psi_p + \mathcal{U}\cos 2\Psi_p)\cos\phi + \mathcal{V}\sin\phi \quad (81)$$

$$\mathcal{V}' = (\mathcal{Q}\sin 2\Psi_p - \mathcal{U}\cos 2\Psi_p)\sin\phi + \mathcal{V}\cos\phi \quad (82)$$

The physical interpretation of these equations is straightforward if we consider the orientation of the Stokes vector in the Poincaré sphere. For a properly calibrated system, the projected components of the Stokes vector onto the (Q,U,V) axes are the values of Q, U, and V, respectively. But for the case considered, where we remain in the antenna frame, and there is a phase offset ϕ between the H and V channels, the observed (primed) values are those obtained by:

- Rotation about the V axis by twice the parallactic angle, $2\Psi_p$, then,
- Rotation about the Q' axis by the angle ϕ, given by the H-V phase offset.

Determination of the phase offset between the parallel-hand channels requires either an introduced calibration signal, or use of an external polarized source. The VLA is not equipped with a suitable calibration signal, so we must utilize an external standard. The determination of the offset is elementary provided we find a strong polarized source with *either* no circularly polarized emission ($\mathcal{V} = 0$), or no linearly polarized signal ($\mathcal{Q} = \mathcal{U} = 0$). In the former case, the H-V phase becomes, from 81 and 82:

$$\tan\phi = -\mathcal{V}'/\mathcal{U}' \tag{83}$$

while for the case of a purely circularly polarized signal, we have

$$\tan\phi = \mathcal{U}'/\mathcal{V}' \tag{84}$$

Note that both of these expressions are independent of the parallactic angle, or of the amount of Faraday rotation the incoming signal suffers. On the other hand, for this method to work, it is necessary there be enough polarized signal in the $\mathcal{U}'$ channel. If the ionospheric RM is such that the value of $\mathcal{U}'$ is zero at any particular frequency, the phase offset cannot be discerned. In general, it is clear that a modest rotation in the Stokes vector (caused either the the intrinsic RM, or the ionospheric RM) will be useful to ensure there is sufficient apparent $\mathcal{U}'$ in most of the spectra windows across P-band to enable a clean determination of the cross-hand phase.

An ambiguity remains – equation 83 provides the same solution if the signs of both $\mathcal{U}'$ and $\mathcal{V}'$ are negated – i.e., we cannot tell if the solution is ϕ, or $2\pi - \phi$. Application of the wrong value negates the sign of $\mathcal{U}$. The solution to this is to have knowledge of the RM of the calibrator source – examination of the derived polarization of the calibrator as a function of frequency will reveal whether the correct sign of the phase has been selected.

At P-band, there are few polarized sources which can be used for this purpose. However, testing has shown that 3C345 is linearly polarized at the $\sim 2\%$ level – the ~ 180 mJy of polarized flux is sufficient. However, the moderately high RM of this source ($\sim 20\mathrm{rad/m}^2$) introduces complications in coherently summing the signal over a frequency span large enough to detect the polarized flux. The hotspots of many radio galaxies are known to be highly polarized at low frequencies – the northern hotspot of DA240 is $\sim$20% polarized, and the western hotspot of 3C303 is $\sim$5% polarized, respectively. However, both are resolved at some level, which may preclude them for use at the VLA's highest resolutions. Full-resolution observations of these, and other potential hot-spot sources will be needed to establish a suitable network of calibrators.

5.4 Comparison to the Circular Case

It is instructive to compare this result to that for a circularly polarized system. Under the same assumptions – that the parallel-hand amplitudes and phases are properly calibrated, that there is no leakage ('D-terms') between the signal channels, and there is a phase offset between the parallel-hand channels, the cross-hand visibilities are given by

$$2R'_{r1l2} = e^{-i\phi}[\mathcal{Q} + i\mathcal{U}] \tag{85}$$
$$2R_{l1r2} = e^{i\phi}[\mathcal{Q} - i\mathcal{U}]. \tag{86}$$

where again the parallel-hand visibilities are unaffected. Forming the apparent visibilities, we get

$$\mathcal{I}' = \mathcal{I} \tag{87}$$
$$\mathcal{Q}' = \mathcal{Q}\cos\phi - \mathcal{U}\sin\phi \tag{88}$$
$$\mathcal{U}' = \mathcal{Q}\sin\phi + \mathcal{U}\cos\phi \tag{89}$$
$$\mathcal{V}' = \mathcal{V} \tag{90}$$

In this case, the visibilities are again modified by a simple rotation, but now the rotation is about the 'V' axis, so the effect is indistinguisable from a sky rotation. Hence, the correction of cross-hand phase can be combined with that due to parallactic angle and Faraday rotation – a considerable convenience.

5.5 Dipole Misalignment and Polarization Leakage

We noted in Section 4.1 that the effects of dipole misalignment and electronic coupling of signals between the electronic chains are the same – both transfer signal from one polarization plane to the other. In the analysis, the effects have been combined, so the cross-hand responses (presuming all parallel-hand calibration is completed and applied) – but remaining in the antenna frame – are, for an unpolarized source,

$$R'_{vh} = \mathcal{I}(T_{hv1} + T^*_{vh2})/2 \quad (91)$$
$$R'_{hv} = \mathcal{I}(T_{vh1} + T^*_{hv2})/2 \quad (92)$$

(the primes indicate the data are calibrated), and where

$$T_{hv} = D_{hv} + \tan\theta \quad (93)$$
$$T_{vh} = D_{vh} - \tan\theta \quad (94)$$

This tells us that the 'leakage' combines a constant offset – in frequency and for both polarizations – due to the misalignment and a variable (in both frequency and between polarizations) due to the subsequent coupling between signal chains. The constant offset P is related to the misorientation by $P = \arctan\theta$. The negative sign of the tangent of equation 94 tells us that the phase of the constant offset will be 180 degrees from that of the opposite hand.

These equations are identical in form to those currently utilized for determination of the leakages in the VLA's circularly polarized systems, in the case where the calibrator is known to be unpolarized. Hence, the same software can be utilized, providing that the software is not asked to solve for source polarization.

In fact, the current polarization software does not solve for these *absolute* values of the leakages, but rather for *relative* values, referenced to a reference antenna/polarization. Experience has shown that this is an adequate approximation for most polarimetric work. If high-fidelity polarimetry (roughly defined as fidelities greater than $\sim 10^4 : 1$, then the absolute values will be needed – a considerably more difficult calibration requirement.

Ideally, all our antennas would have correctly oriented, orthogonal dipoles. In this case, an unpolarized source will provide no cross-hand amplitudes. Hence cross-hand calibration requires a significantly polarized source – as noted above, there are few such sources known, and those that are may be resolved out at our highest resolutions. The alternative is to deliberately misalign at least one antenna's dipoles. Ideally, this would be a rotatable feed, so the dipoles would be rotated to allow calibration, then re-aligned for astronomical obserations. Note that the angles determined (via the offsets in the solutions) are actually the angle offsets from the reference antenna. It is thus critical that the reference antenna be correctly oriented.

5.6 Gain Application – Determination of the Stokes Visibilities

Once all the required calibration values are determined, the Stokes visibilities can be determined, utilizing equation 51. It is of critical importance that the application of the calibration follow the order shown in that equation – namely:

1. The parallel gains (including the cross-hand delay and H-V phase).
2. The corrections for misalignment of the dipoles and signal change leakages.
3. The rotations due to the parallactic angle and ionospheric rotation.

Any change in the order will result in incorrect values of the Stokes' visibilities.

Note that the effect of ionospheric rotation can be accommdated – if known – during the last stage, where the effects of antenna paralactic angle rotation are accounted for.

6 On-Sky Verification

To demonstrate that we have correctly described the relations, and that our recommended calibration regimen is correct, we have conducted observations of radio sources with known polarization with the VLA's new 'Low-Band' system.

6.1 Choice of Calibrators

Two types of calibrators are required for full characterization – unpolarized calibrators for the establishment of parallel and cross-hand gains, and at least one polarized source to measure the cross-hand (H-V) phase.

Within the P-band system, the choice of unpolarized calibrators is quite simple. The strong, well-known calibrators 3C147, 3C295 and 3C286 are polarized at much less than the 1% level. More difficult is the selection of polarized sources strong enough to be detected with good SNR. The well-known high-frequency calibrator 3C345 (J1642+3948) is weakly polarized at P-band, and we have included this source in the observing program.

Pulsars are known to be strongly linearly polarized at meter wavelengths. We have attempted to utilize pulsars as polarization calibrators, but without useful results, as the period-averaged flux is too low for reliable detection. The SNR can be greatly improved by utilizing the pulsar phase binning modes but, as we are seeking a simple calibration method which is applicable to general continuum observing, we have decided to eschew these exotic observing modes.

The only other class of sources strongly polarized at low frequencies are the compact bright hotspots of radio galaxies and quasars. Noting that the WSRT has successfully utilized the eastern hotspot of DA240, we have included this source. A literature search also identified the western hotspot of 3C303 as a potential source of polarized flux. A likely drawback of these targets is their resolution – hotspots are typically resolved on arcsecond scales, so that their use in the A configuration is not at all assured.

6.2 Choice of Target Source

To prove that our relations and procedures are correct, an observation of sources of Finally, an observation of a source of *known* polarization is essential. Although various radio galaxies may suffice, we are not sure of the polarization structure, as these sources are likely to be depolarized at lower frequencies and lower resolutions due to Faraday effects and/or beam depolarization.

Thus we seleccted the moon as a suitable target source. As a thermal object, with no atmosphere and no ionized screen, the polarization structure is absolutely known without concerns of Faraday depolarization. The cause of the polarization is the reflection of the upwelling thermal radiation upon crossing the lunar surface to free space. The two orthogonal planes of polarization have different reflection coefficients, thus leading to an apparent, radial, linearly polarized emission which rapidly increases with offset from the lunar center. Perley and Butler (2014) have described the relevant physics of this process, and show that the maximum fractional polarization at the limb exceeds 30%. The downside of this source is that the moon is very large (30 arcminutes diameter) and dim – only ∼220K brightness, corresponding to about 60 Jy total flux at 420 MHz over the entire disk. The background sky brightness is typically 20K at these frequencies, but reaches values equal to the brightness of the moon in the vicinity of the galactic center. Care must be taken to avoid observations when the moon transits the galactic plane near the galactic center – the total intensity (but not the polarization) will disappear during this transit!

6.3 Observations

There were three observing sessions, but only the third was actually utilized for the analysis shown in this memo. We briefly summarize the results of the first two observations. The first, 6 hours on 10 May 2017, was in D configuration. It was focused mostly on finding calibrators – specifically, to determine if the pulse-averaged polarized flux from a number of pulsars was sufficient to enable their use as calibrators. The short answer is 'no'. This run was also useful in showing that the ephemeris used (by both AIPS and CASA) was incorrect – the initial images of the moon showed it to be highly elliptically elongated. It was also determined that D configuration is not optimal for this work – the RFI is too strong, and the resolution not high enough to clearly show the desired lunar polarization.

The second test, taken on 06 August, 2017, comprised 8 hours in C configuration. This time, the moon was close to the galactic plane, reducing its contrast against the bright background. It was also at an RA that prevented observation of DA240, by far the best polarized source. Nevertheless, the data were sufficient to show that the H-V phase offset was critical to establish proper imaging, and that a strongly polarized calibrator was essential to determining this quantity. But, with only 3c345 as the polarized source – which as will be noted later also has high rotation measure, it was difficult to determine the phase offset.

The third, and final test benefited from the lessons learned from the first two experiments. This run comprised a full 12 hours in C configuration on December 30, 2018, starting at 01:10 MST. The LST start time was 07:40. The moon at the beginning of the run was near RA=13:25, Dec = 03:31, and at the end was near RA=13:43, Dec = -05:55. All sources were observed for the maximum time permitted by the 8 degree elevation limit. A summary of the observations is shown in Table 1

Table 1: Observing Log

Source	Nobs	On SourceTime min	HA Range deg	Δ PA deg	Elev Range deg
DA240	8	6	0 →119	90	16 – 68
3C147	6	3	30 →105	55	17 – 63
3C286	14	7	-87 → 88	55	19 – 82
3C303	14	11	-105 → 65	220	18 – 72
3C295	14	7	-97 → 77	220	22 – 72
3C345	11	11	-105 → 40	215	11 – 81
3C273	51	27	-66 → 81	120	11 – 58
Moon	59	435	-80 → 75	120	8 – 52

Three unpolarized calibrators were observed: 3C147, 3C295, and 3C286, approximately once an hour when they were visible. Three known polarized sources were also observed: DA240, 3C303, and 3C345. The target source was the moon, on which the great majority of the time was spent. The moon's local calibrator chosen was the very strong quasar 3C273, which was only ∼12 degrees away. (Indeed, 3C273 was occulted by the moon on the previous day).

The correlator mode was set to the standard 4/P setup – the P-band portion utilized 16 spectral windows, each 16 MHz wide, with 250 kHz spectral resolution. Hence, there were 64 channels per spectral window, and 1024 channels overall, per polarization product. The total frequency span was 256 MHz, spanning 232 to 488 MHz.

The data were taken in C configuration – which is about optimal for retaining sufficient short spacing to image the moon's disk in Stokes 'I', while having enough resolution to clearly show the edge-brightened polarization structure.

RFI is a significant issue at P-band, particularly in the C and D configurations, where the low fringe rate gives rather poor rejection of stationary sources of interference. Rather than spend much time purging the worst RFI, we took the simpler path of utilizing only half the bandwidth, corresponding to two spectral regions, comprising four contiguous spectral windows, which are relatively free of RFI. Hence, spectral windows 5 through 8, and 11 through 14, were extracted, and processed separately. These correspond to frequency spans 288 MHz through 352 MHz, and 384 MHz through 448 MHz.

6.4 Calibration

The calibration regimen is described below.

- The AIPS task `SPLAT` was used to Hanning smooth the raw data, and to extract the two pairs of four spectral windows. The spectral smoothing is necessary as the Gibbs' ringing (due to the sharp cutoff in the lag function) spreads RFI over many channels.

- Although the chosen sets of spectral windows are relatively free of serious RFI, some is seen. The tasks `UVFLG` and `CLIP` were employed to flag channels and times with detectable RFI. The process of effectively removing RFI is necessarily iterative – since calibration is affected by RFI, and the level of RFI is affected by calibration, one must proceed in steps, removing the most visible RFI, then calibrating, followed by more RFI removal, etc.

- The parallel hand delays were solved for with `FRING` on the major calibrators (3C147, 3C295 and 3C273). Antenna ea03 was utilized as the reference, as it was located on the end of the west arm. Using an end antenna is useful at these low frequencies as there are few short spacings to these antennas, which reduces the effects of RFI and large-scale background emission in the solutions. `FRING` also provides parallel-hand phase solutions. The phase stability was exceptionally good this day. Examples of the phase solutions (w.r.t. ea03) are shown in Fig 2. The delay and phase solutions are recorded in the `SN table`, and were applied to the `CL` table with `CLCAL`.

- The bandpasses were solved for using `BPASS`, again with ea03 as reference, and using the observations of 3C295. The solutions for two antennas are shown in Fig 3. The small-scale (3 MHz) oscillations are due to cable reflections.

- The flux density scale of Perley & Butler (2017) was utilized through `SETJY` for 3C147, 3C295, and 3C286.

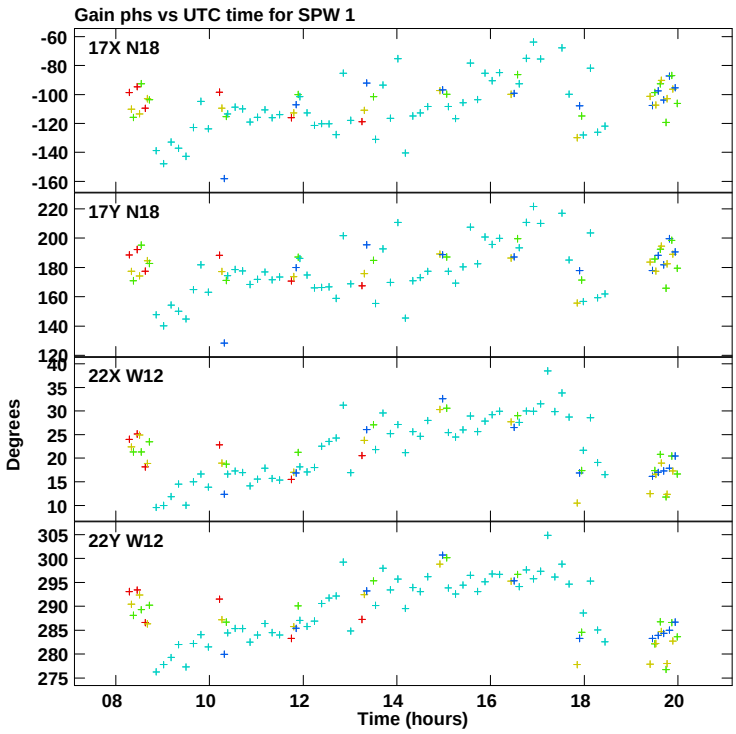

Figure 2: The phase solutions for two typical antennas – ea17 at N18 represents a long baseline, and ea22 at W12 a short baseline. The reference antenna was ea03, at the end of the west arm (W18). The phase stability was very good. The various sources are color-coded – 3C147 is red, 3C273 in blue, 3C295 in green, and 3C286 in yellow.

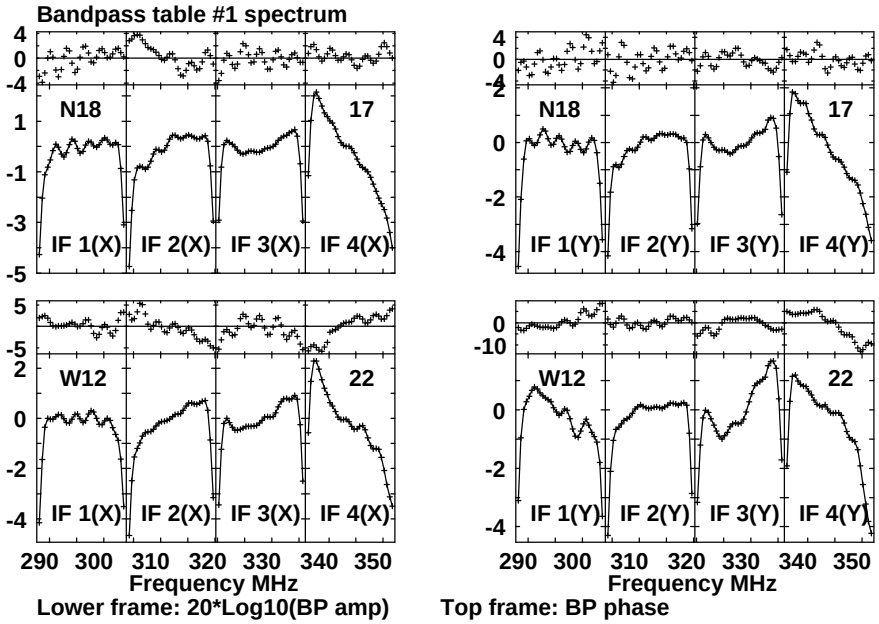

Figure 3: Normalized bandpass solutions for two antennas, ea17 and ea22, for the lower set of four spectral windows, spanning 288 through 352 MHz. The phases are in the upper (narrow) panels, the power bandpasses below, in dB. The phases average zero with zero slope since the parallel hand delays were derived in the previous step.

- Parallel-hand calibration was next, using the unpolarized sources 3C147, 3C273, and 3C295. Because 3C273 is slightly resolved (about 18 arcseconds, or 1/3 the synthesized beam), a model is needed in order to utilize this source for local calibration. Hence, the data for this source were extracted, and a few round of self-calibration provided the needed models for both data sets. The solutions were determined using `CALIB`, and applied with `CLCAL`. In Fig 4 shows typical solutions.

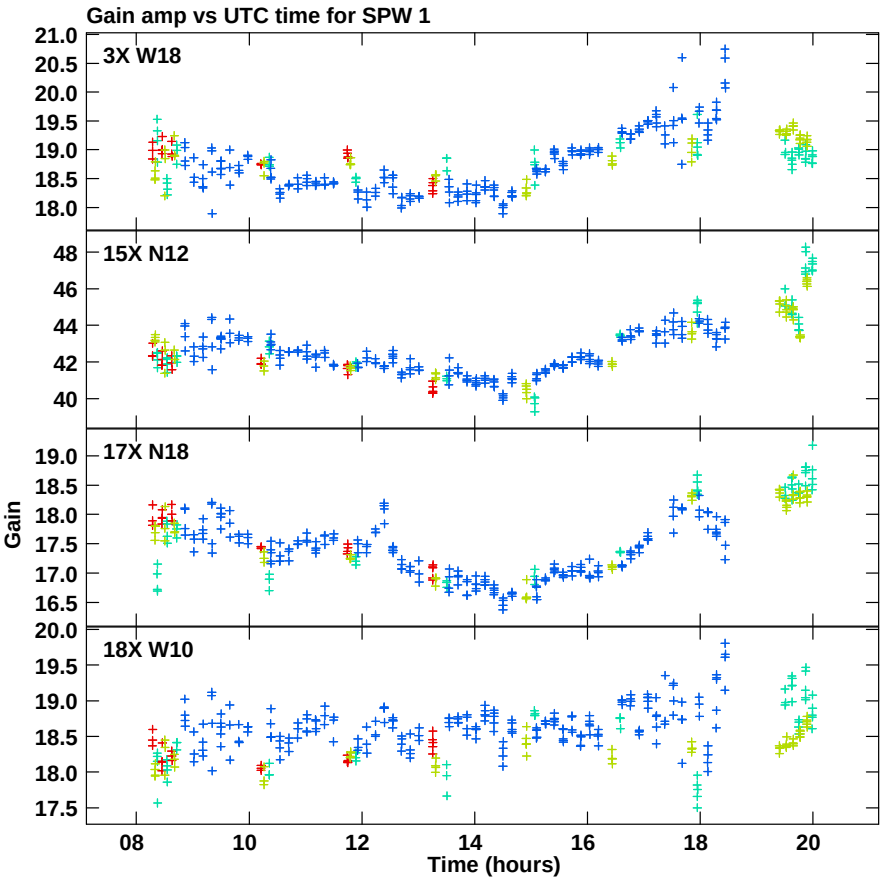

Figure 4: Amplitude gain solutions for four antennas. The plotted values are color-coded: 3C147 in red, 3C273 in blue, 3C295 in green. For most antennas, the gain stability is very good.

- The determination of the cross-hand phase is next. There are two stages – removal of the cross-hand delay, then the determination of the residual phase. (a) `RLDLY` was run using the unpolarized sources 3C147 and 3C295 to determine the cross-hand delay. The solutions are applied with `CLCOR`. There then remains a single phase offset. To determine this, the program `XYDIF` determines the apparent (without parallactic angle correction) values of U and V, and implements equation 83 to find the cross-hand phase. Alternatively, one can generate U and V images of the highly polarized sources when Ψ_p is 0 or 180, determine from these the value of the phase, and apply the phase with `CLCOR`.

- The final step is to determine the cross-hand leakages – caused both by the dipole misalignment and actual 'D' terms coupling the parallel-hand signals. This was done by using `PCAL` on the unpolarized sources 3C147 and 3C295. Example solutions are given in Fig 5. The constant offsets, seen at the 10% level in the lower panels (ea20), are given by $\tan\theta$, and are the same for all frequencies. The 'oscillations' about the offsets are the actual D-terms, caused by electronic or radiative coupling between the parallel hand signals.

This concludes the calibration. The required visibilities corresponding to the Stokes I, Q, U, and V are formed by applying equation 51. We emphasize again that it is critical that the gain corrections described above be applied in the proper order – namely, working backwards from correlator to sky. Thus:

- The parallel-hand gains (including the cross-hand phase) are applied first to the correlator data.

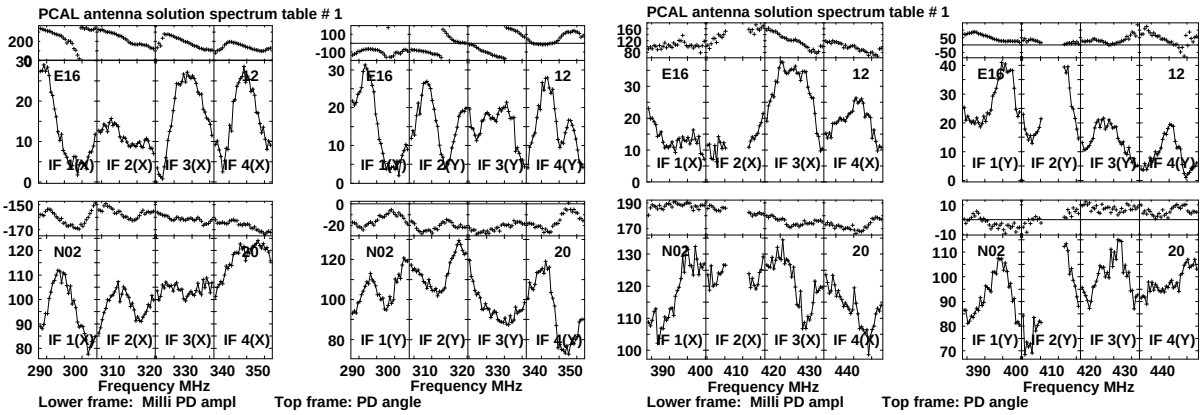

Figure 5: The cross-polarization 'leakages' for two antennas, and both frequency sets. The values shown are in tenths of percent. For all antennas, the solution amplitudes have an average value which is the same for both polarizations and all frequencies, with fluctuations about this value. The constant offset is equal to $\tan\theta$, the misalignment angle (w.r.t. the reference antenna). The variations are due to radiative or electronic coupling between the orthogonal signal chains. Note that, for ea20, which has a high mislignment (5.5 degrees), the phases of the two polarizations differ by 180 degrees – as expected. For ea16, which is well aligned with the reference antenna, the phase solutions show no such relation.

- The polarization mixing matrix inverse (T-terms, combining both misalignment and true leakages) are applied next.
- The parallactic angle rotation (and ionospheric angle, if known) are applied last.

6.5 Imaging

Here we describe the results from imaging of the calibrators and target source.

6.6 Calibrator Polarization Characteristics

Images in I, Q, and U were made for the three polarized calibrators – DA240, 3C303, and 3C345. Significant polarization was found from all three: For 3C303, the fractional polarization (originating from the western hotspot) is 4% in the lower frequency window, and 4.5% in the upper window. For DA240, the polarization is remarkably high – 18% for the lower frequency window, and 22% for the upper. For 3C345, it is 1.8% in the lower window, 2.1% in the upper.

Each has a significant rotation measure, so images were made with an appropriate frequency spacing in order to determine the RMs. The results are shown in Fig 6

6.7 RM Variation over Time

The ionosphere is a very dynamic medium, causing typically one radian of rotation to the plane of polarization. The excellent phase stability noted above is an encouring sign that the ionosphere was quiescent throughout the run. To check that this extended to the RM, we made 'snapsnot' images of the highly polarized hotspots of DA 240 and 3C303 at 327 MHz. The results are shown in Table 2. Columns 2 through 4 are the elevation, parallactic position angle, and observed polarized flux position angle for DA240. Columns 5 through 7 are the same for 3C303. We note that the differential rotation through the ionosphere was indeed quite small – merely 8 degees for DA240 (observed through the night into early morning), and about 20 degrees for 3C303 (observed throughout the 12-hour run, from 1AM to 1PM, local time). Such a rotation will have only a small effect on the polarized images of the moon.

6.8 Images

Images of the point-source calibrators are interesting only in their display of the background sources extending out to ~ 6 degrees. None warrant display here. Two sources are extended enough to be interesting. The first is DA240,

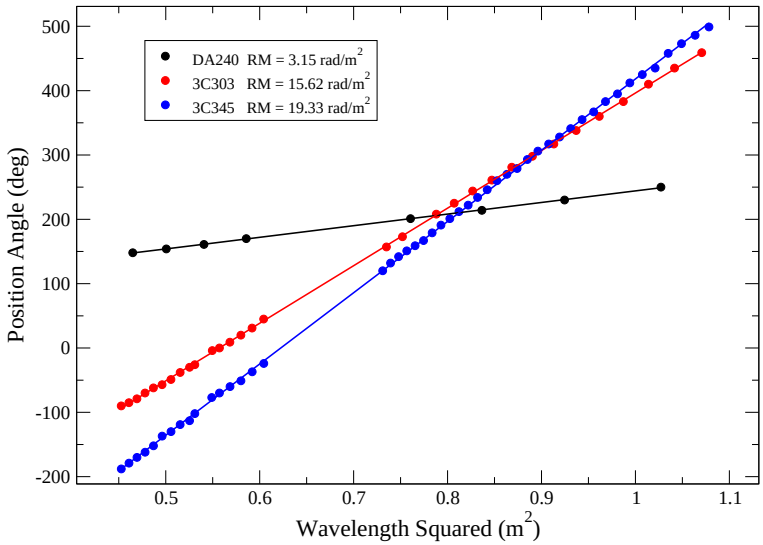

Figure 6: The observed position angle of linearly polarized flux for each of the three known polarized sources. The formal error in the fits is ± 0.03 rad/m^2. The vertical offsets are arbitarary, as the zero-wavelength position angles are unknown.

Table 2: Observed Position Angles for DA240 and 3C303

Time IAT	El deg	PA deg	χ de	El deg	PA deg	χ deg
8:14	68	-173	68			
8:20				18	-58	5
8:23	68	-178	69			
8:30				19	-59	10
8:34	68	176	70			
8:40				21	-61	11
10:10	62	130	72			
10:16				35	-77	11
11:40	50	102	69			
11:49				49	-95	9
13:12	38	83	67			
13:18				62	-119	11
14:50	24	67	69			
14:55				72	-165	6
16:20	16	48	64			
16:27				68	139	-10
17:51				57	108	-14
19:24				43	87	-7
19:33				42	86	-4
19:40				41	84	-4
19:47				39	83	-2
19:54				38	82	-1

a nearby (z = 0.0357) giant radio galaxy with unusually extended lobes and an extremely bright hotspot in the north-eastern lobe. The full extent of this source is about 1.2 Mpc. It is this extremely bright hotspot which is highly polarized – at about 20%. Shown in Fig 7 is our image, made using the lower frequency band. Weak polarized emission is also seen in the lobes. This is a remarkably good image, given that it is based only six minutes of on-source integration!

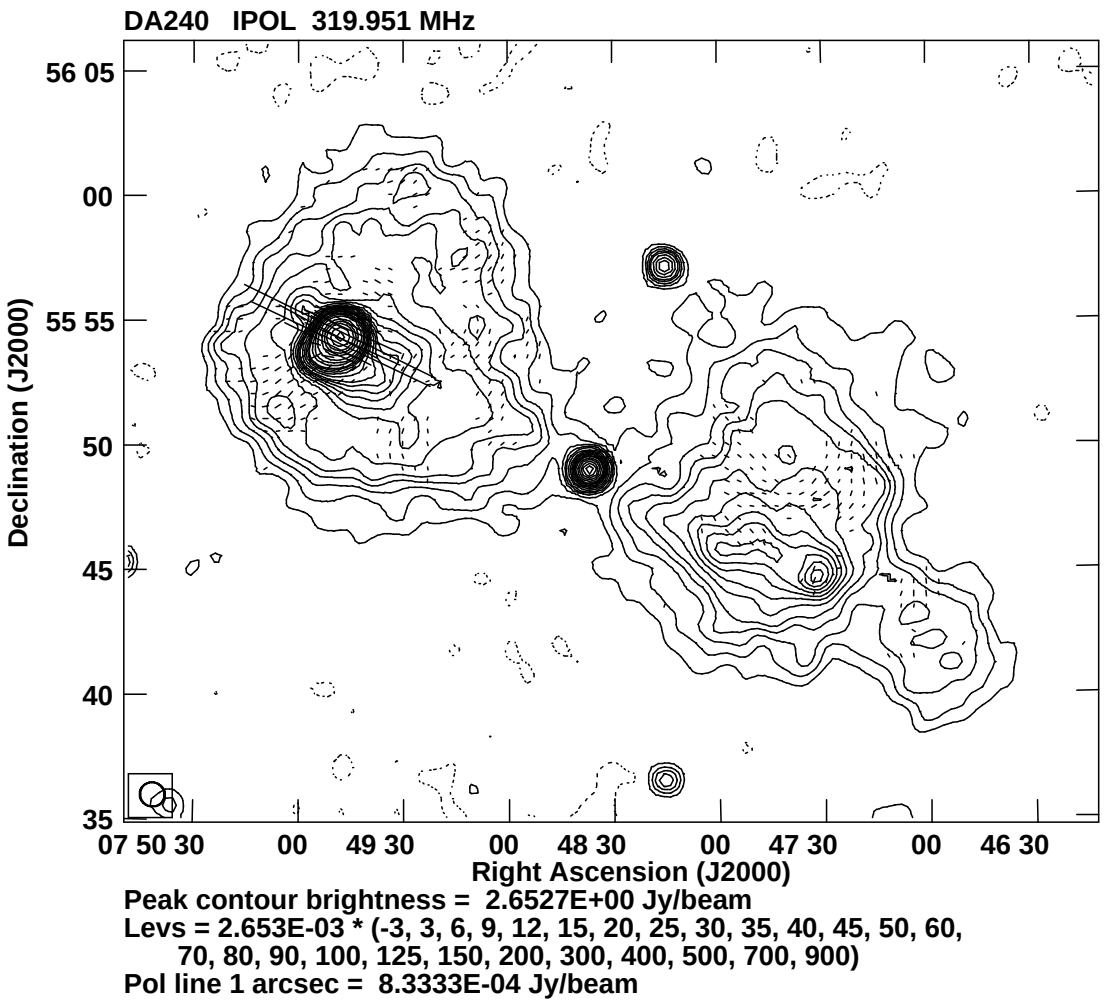

Figure 7: The radio galaxy DA240 at 320 MHz, with 59 arcsecond resolution. The polarization dashes show the polarized intensity. The hotspot is extremely bright in polarized light. Weak, but significant polarized brightness is detected in both lobes. The observed hotspot RM of 3.15 radm^2 was utilized to allow coherent integration over frequency of the Q and U images for the whole source, but the angles shown are arbitrary as the rotation due to the ionosphere has not been applied. Only six minutes of on-source data were utilized.

The 'proof of the pudding' is in the images of the moon, since for this source, we know in advance what the polarized emission must be. Shown in Fig 8 are two images of the moon's polarization and total intensity. The left figure shows these at 321 MHz, the right at 417 MHz. The position angles shown have been rotated by -25 and -40 degrees, respectively, to align them with the known angle of emission for polarized light from the rim of the moon. These two values are consistent with an $RM = -0.7\,\mathrm{rad/m^2}$ – a very reasonable value for the quiescent ionosphere.

More striking are the individual images for the four Stokes parameters, and the polarized images, shown in Fig 9. The upper left panel shows the Stokes 'I' image. The brightness contours are tiled along a SE – NW axis, the major axis of which points towards the sun. The polar regions are notable cooler than the equator, as expected. The observations were taken near first quarter, so the left side of the sun was illuminated, while the right side was in darkness. Due to the depth from which this radiation originates at these wavelengths (a few meters), there is no strong E-W asymmetry noted in this image. Near the SE limb is an isolated bright spot of emission, whose origin is discussed below.

The central and upper right images in the figure show the Q and U images (not rotated for the ionopheric rotation). These clearly show the expected pattern for a radially oriented polarized structure, whose amplitude rises towards the rim. There is a weak maximum in the center – due to reflected signals of terrestrial origin.

The lower left image shows the Stokes 'V' brightness. There is no detectable signal except for a broad central

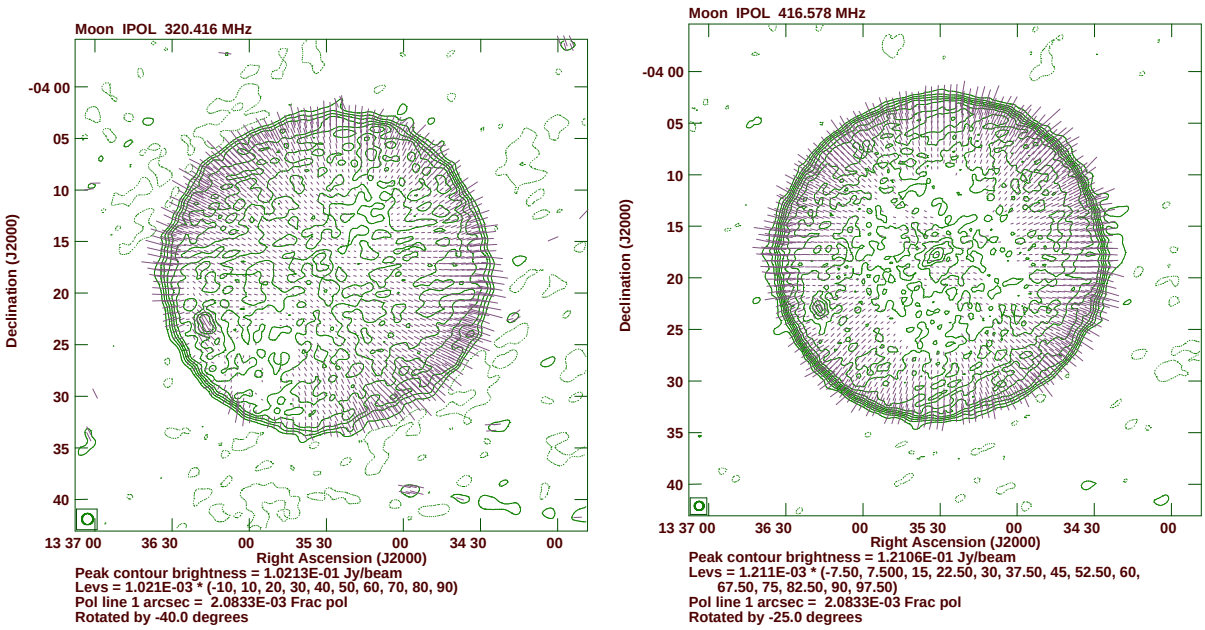

Figure 8: The moon's polarized and total intensity. The left panel shows the emission at 321 MHz, the right panel shows it at 417 MHz. The polarization vectors at the lower frequency have been rotated by -40 degrees, those at the higher frequency by -25 degrees. These are consistent with an ionospheric RM of -0.7 rad/m^2.

region. This can only be due to reflected emission from the earth – although the apparent extension does not have an obvious explanation. The sign and strength of the emission varies with frequency.

The total linearly polarized brightness $P = \sqrt{Q^2 + U^2}$ is shown in the middle lower panel. This shows the expected sharp rise in polarized brightness towards the limb. In the lower right panel is shown the percentage polarization. The maximum of 30% is very near the theoretical maximum.

The local maximum in total intensity near the SE limb noted above is seen to have a corresponding maximum in polarized intensity. Reference to figure 8 shows the the plane of polarization from this 'spot' is exactly orthogonal to that of the lunar thermal emission, and is thus oriented perpendicularly to the line joining this maximum to the disk center. The brightness location and polarization is clear evidence of this being reflected emission from the sun.

The moon's emission is known to be thermal, hence the brightness temperature should be constant over frequency, so the lunar flux density ($S = \frac{2kT\nu^2\Omega}{c^2}$) should scale with ν^2. To check this, we made images in each of the eight spectral windows. In the analysis, we must adjust for the bright galactic background, which is sharply rising with increasing wavelength. Since the interferometer is sensitivie to the brightness difference between the background and the moon, an approximate procedure is to calculate the occulated background flux, and add this to the observed flux from the moon. The results of a simple analysis are shown in Table 3 We see from this simple (and approximate)

Table 3: Lunar Flux Density and Brightness

Freq MHz	Obs. Flux Jy	T_{bg} K	S_{bg} Jy	Adj. Flux Jy	T_b K
296	20	64	21	41	237
312	26	56	19	45	226
328	31	49	16	47	222
344	35	44	12	47	242
392	58	29	10	68	214
408	61	27	9	70	210
423	70	24	8	78	213
440	76	22	7	83	223

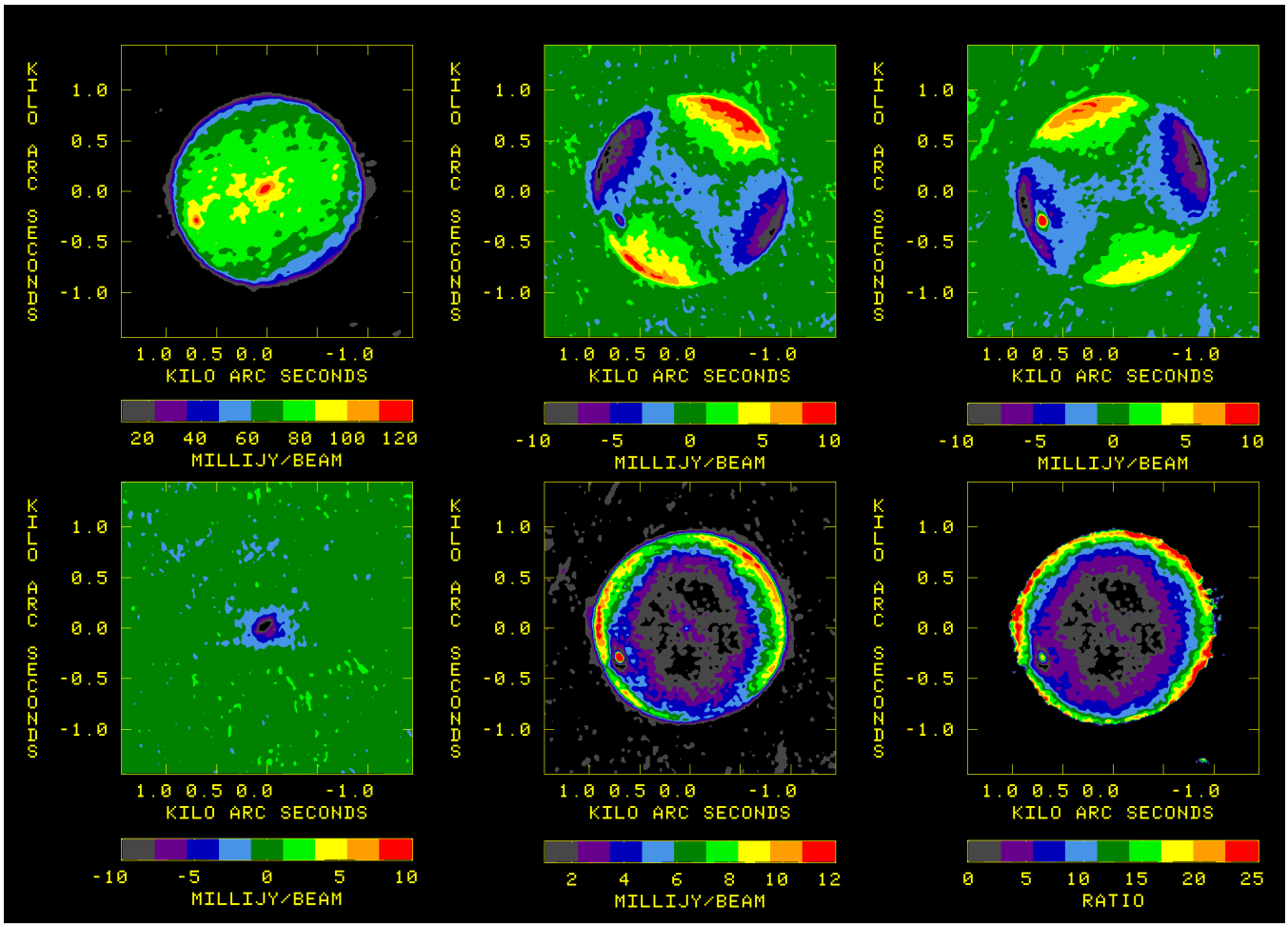

Figure 9: Color representations of the lunar emisssion at 415 MHz with 52 arcseconds resolution. Top row: I, Q, and U. Lower row: V, Polarized intensity P, and percentage polarization P/I.

analysis that the occulted flux at the lower end of this experiment becomes a significant fraction of the total lunar emission, but after accounting for it, the lunar disk brightness temperature is indeed close to constant across the observed spectral span.

7 Conclusions, Comments, and Acknowledgements

We have derived the relations between the observed visibilities and the desired Stokes visibilities for the VLA's linearly-polarized P-band receivers. Observations of the moon have shown the correctness of our formalism. The calibration regimen has been established, so that the VLA's P-band system can now be used for polarimetry. Missing from our treatment is any discussion of correction for ionopheric rotation – this is beyond the scope of this document.

Although we are confident in the correctness of this work, much work remains to make P-band polarimetry easy for the users.

- A larger list of suitably polarized sources needs to be established in order to enable measurement of the cross-channel phase. It is highly unlikely that any of the current flat-spectrum sources used in calibration will have enough polarized flux to be useful. Since DA240 and 3C303 contain highly polarized hotstpots (and we know that Pictor A does also), a survey of suitably strong and compact hotspots is needed to find more polarized sources.

- The stability of the H-V phase needs to be established. As this is an instrumental effect, we might hope that it is relatively stable over time. (The same statement should hold for the R-L phase difference for the circularly

polarized receivers at the other VLA bands – however, to our knowledge, no study has ever been undertaken to establish the truth of this.)

- A method to unwrap the rotation due to the ionosphere will be needed. We were fortunate that our crucial third test was done with a quiescent ionosphere. Future observations will not be so fortunate. Such studies of ionospheric corrections are being undertaken in the Netherlands to support LOFAR – we should learn from this work.

7.1 Linear vs. Circular

A number of useful lessons were learned about dealing with linearly polarized feeds. We outline these below, along with some comments comparing these to circular.

- Accurate parallel-hand calibration requires knowledge of the polarized state of the calibrators. This is because the linearly polarized flux is coupled directly to the parallel-hand correlations. For meter-wavelength observations, this is not a serious problem, but for cm-wavelenths, the situation is different. Since most of our calibrators at cm-wavlengths are polarized at the few % level – and are variable – their polarization state must be known for accurate calibration to be effective.

- For observations requiring many hours, existing methods for calibration, utilizing the rotation of the sky w.r.t. az-el mounted antennas, are effective in determining calibrator polarization. However, for 'snapshot' instruments (2-dimensional arrays, such as the VLA and planned Next Generation VLA), this convenient method is not available, so calibrator polarization will need to be known for accurate calibration to proceed.

- Perhaps the most serious concern regarding use of linearly polarized receivers is their effect on self-calibration. In this process, a reasonable estimate of the image brightness is utilized to estimate the gain adjustments needed to improve the fidelity of the image. Nearly all the spectacular results of this process have been generated using VLA data. For the circularly polarized receivers of the VLA, the process is simple, as the parallel-hand correlations are sensitive to only I and V – and for nearly all sources, V is negligible, so only an I image is needed. For a linearly polarized receiver system, the process of self-calibration will be much more complicated, as reasonable estimates of the linear polarization of the target source will also be required for the calibration process to proceed. Since most targets for high-fidelity images will be linearly polarized (in some cases, strongly so), this is an important complication that must be considered.

It has often been pointed out that any orthogonal pair of receiver polarizations (opposite circular, orthogonal linear) are sufficient for full polarimetry to be enabled. While this is true, what is not often appreciated is that the differences between circular and linear polarizations are manifest in the calibration procedures. With circular polarization receivers, basic calibration is 'dead simple', for the reason that calibrators (and most target sources) have neglible circular polarization. For linear polarization receivers, the process is significantly more complicated. This is indeed a situation where 'the devil is in the details'. So while engineering arguments strongly support linear polarization for its higher sensitivity and engineering simplicity, arguments based on the practicalities of calibration argue for circular. Unsurprisingly, the authors of this memo strongly favor circularly polarized systems.

7.2 What has not been discussed

What we have not discussed in this memo are the efforts required to establish and confirm the relations contained within. To a large degree, these comprise a 'case study' of the surprises and difficulties encountered when a new and unfamiliar capability is enabled. What may seem simple when written down on paper can turn out to be considerably more difficult when the data actually flow, and the various errors and misunderstandings become apparent. A recantation of the trials and tribulations encountered during the testing ('commissioning') of this facility will require a document much larger than this one! Suffice to say that a long list of errors (both in our work, and in that done by others) was encountered and corrected.

7.3 Acknowledgements

This work could not have been successful without the ready assistance of many people. We are thankful for the help and advice given by Barry Clark, most particularly in diagnosing why our initial images of the moon were ellipsoidal! We are grateful to the quick response by Bill Cotton to correct issues uncovered with the OBIT program `BDFIn`,

which is essential to getting VLA data into AIPS. Bryan Butler's quick approval of the observing programs whose data were crucial to understanding the various quirks, is gratefully acknowledged. Bryan also suggested the moon as a suitble standard object. We thank Michiel Brentjens for his advice, drawn from his thesis work on the WSRT. Finally, we acknowledge Justin Bray's assistance in correctly interpreting the reason for the bright spot seen on the SE limb of the lunar emission.